Structural and AC Magnetic Properties of $(Ni_{0.4}Cu_{0.15}Zn_{0.45})_{1-x}Mn_xFe_2O_4(x=0.30, 0.45)$ due to Mn Substitution

A Thesis submitted to

The Department of Mathematics and Natural Sciences, BRAC University, Dhaka, in partial fulfillment of the requirement for the award of the Degree of Bachelors of Science in Applied Physics and Electronics

SUBMITTED

by

ZARRIN TASNIM MRIDULA

ID NUMBER : 13115005

SESSION : Fall 2017

DEPARTMENT OF MATHEMATICS AND NATURAL SCIENCES

BRAC UNIVERSITY, DHAKA 1212, BANGLADESH

CANDIDATE'S DECLARATION

It is hereby declared that this thesis or any part of it has not been submitted elsewhere for the award of any degree or diploma.

_____

Zarrin Tasnim Mridula

13115005

_____

Certified by

Dr. A.K.M Akther Hossain

Professor

Department of Physics, BUET

ACKNOWLEDGEMENTS

The Author

ZarrinTasnimMridula

Table of Contents

LIST OF SYMBOLS AND ABBREVIATION

AC	Alternating current
B	Magnetic induction
$F(\theta)$	Nelson-Riley function
f_r	Resonance frequency
L_s	Self-inductance of the sample core
L_o	Inductance of the winding coil without sample
M	Magnetization
M_s	Saturation magnetization
N_A	Avogadro"s number
P	Porosity
P_{intra}	Intragranular porosity
P_{inter}	Intergranular porosity
Q	Relative quality factor
T_c	Curie temperature
T_n	Néel temperature
T_s	Sintering temperature
$\tan \delta$	Loss factor
Z	Complex impedance
μ_i	Initial Permeability
μ'	Real part of complex permeability
μ''	Imaginary part of complex permeability
x_{spin}	Intrinsic rotational susceptibility
x_w	Domain wall susceptibility
θ	Bragg"s angle

LIST OF TABLES

LIST OF FIGURES:

ABSTRACT

Structural and magnetic properties of $(Ni_{0.4}Cu_{0.15}Zn_{0.45})_{1-x}Mn_xFe_2O_4$ ferrites(x=0.3, x=0.45) were investigated and it was prepared by solid state reaction methods. Various chemical compositions were calcined at 950°C, and samples prepared from these compositions were sintered at 1100°C in air for 5 hours. The X-ray diffraction analysis, SEM and EDS results were performed for the samples sintered at 1100°C temperature. X-ray diffraction pattern confirms the formation of single phase spinel structure and the lattice parameter which resulted in increasing with the increase of Mn^{2+}. The compositions show a decrease in bulk and theoretical density with increase of Mn^{2+} that can be explained by the atomic weights of the doped and substituted elements. It is also observed that porosity increases, while gain size decreases with increasing of Mn content. EDS report shows the homogeneous distribution of elements in the samples. The permeability curves have shown a quite variation while being sintered at different temperatures. However, the real part is always higher for all temperatures when Mn is absent from the composition. With each content increment, real part of permeability decreases with x=0.3 to x=0.45 at 1100, 1150 and 1200^0C. Natural resonance frequency is noticed to be decreased with temperature rising, although it rises with increasing Mn content.

CHAPTER 1

Introduction

1.1 General Introduction

The term „Ferrite‟, derived from the Latin word for iron, refers to groups of material based on iron oxide. Such iron oxides generally consists of the structural formula: MO. Fe_2O_3, where M denotes metal ions (e.g. Mn^{2+}, Fe^{2+}, Co^{2+}, Ni^{2+}, Cu^{2+}, Zn^{2+}, etc.). Around 1945, Snoek et al [1] introduced and augmented the ferrites by carrying out series of intensive researches at the Philips Research Laboratories in Holland. His studies were later propelled by Louis Néel [2], a French physicist who also enhanced greater theoretical understanding on ferrites. He won the Nobel Prize for his fundamental work and discoveries concerning anti-ferromagnetism and ferrimagnetism which have led to important applications in solid state physics in 1970s.

The high resistivity of ferrites ranges from 10^2 to 10^{10} ohm-cm depending on their different chemical combination which is roughly 15 orders of magnitude higher than that of iron [3]. Such high resistivity contributes to low eddy current losses making these materials very useful in microwave devices and memory core elements. Besides, Ferrites also exhibit ferrimagnetic properties below the Curie temperature, indicating that they own intrinsic resultant magnitude of magnetic moments before turning themselves into paramagnets with weak or no magnetic field over the Curie temperature [4].

Spinel type ferrites are generally utilized in many magnetic and electronic devices due to their high magnetic permeability [5] and also used in electrodes for high temperature applications because of their high thermodynamic stability, electrical resistivity, electrolytic

activity and resistance to corrosion [6]. Not only that, these low cost materials is easy to fabricate and offer the advantages of greater shape formability than their metal and amorphous magnetic counterparts. Almost every item of electronic equipment produced in the modern world today contains some ferrimagnetic spinel ferrite materials. Loudspeakers, deflection yokes, motors, radar absorbers, electromagnetic interference suppressors, proximity and humidity sensors, antenna rods, recording heads, inductors, etc are frequently based on ferrites.

1.2. Objective of the Research

Ferrite compositions which are suitable for miniature cores and the ones that require low temperatures operating at high frequencies are being required for technological progresses all throughout the world. As Manganese in supposed to enhance the ferrite composition with increased permeability, assessment is done to study the structural, magnetic and other characteristics changes that happens with different temperatures.

1.3. Possible Outcome of the Research

Permeability of the ferrite sample is expected to increase because it is being doped with Mn. Other than that, enhancement of grain size, less porosity and impurity may be achieved from the experiment.

1.4. Summary of the Thesis

Summary of the thesis is as follows:

Chapter 1-Introduction and objective of the research

Chapter 2-Provides basic information on ferrites, their structures and permeability mechanism

Chapter 3-Details of sample preparation and experimental techniques

Chapter 4- Results and discussion

Chapter 5- Conclusions and recommendations for future research.

CHAPTER 2

Literature Review

2.1 Overview of the Materials

Ferrites are also referred to as a group of ceramic/non-metallic compounds composed of Iron and other metal oxides in different proportions that drives or determines their physical, chemical, electrical and magnetic properties. Not only that, method of preparation, substitution and doping of different cations, sintering temperature and time, sintered density, grain size and their distribution decides the properties of such ferrites [8, 9]. Tasaki et al. [16] studied the effect of sintering temperature and found out that high density contributes to higher permeability. Nakamura [17] suggested that both the sintering density and the average grain size increased with sintering temperature due to variations in magnetization, initial permeability and electrical resistivity. Roess [18] claimed that attainment of high permeability is restricted to certain temperature ranges.

After Hilpert (1909) focused on the usefulness of ferrites at high frequency [8], Sonek''s hard work unveiled many mysterious magnetic properties of ferrites while he was looking for high permeability materials of cubic structure. He found suitable materials with high permeability in the type $MeZnFe_2O_4$, where Me stands for metals like Cu, Mg, Ni, Co or Mn [8, 14-15]. Ferrites are really crucial in the field technology as they are hard, brittle, polycrystalline,

nonmetallic with intrinsic magnetic properties, etc. Ni-Cu-Zn based ferrites are soft ferrites that have low coercivity which indicates that the material"s magnetization can easily be reversed without significant energy losses. Besides, comparatively low losses in high frequencies make them really useful in electronic devices [7].

2.2 Ferrites and Spinel Structures

Spinel structure is very common in ferrites having the general formula of AB_2O_4 where, the divalent cations like Mg, Cr, Mn, Fe, Co, Ni, Cu, Zn, Cd, Sn, etc. occupy the tetrahedral voids whereas the trivalent cations like Al, Ga, In, Ti, V, Cr, Mn, Fe, Fe, Co, Ni, etc. occupy the octahedral voids in the close-packed arrangement of oxide ions. Bragg and Nishikawa [8, 19] first determined such crystal structures. The following figure represents the schematic of Spinel Structures:
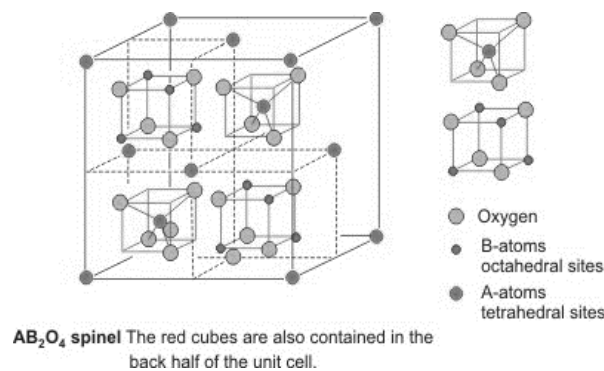
Figure 2.1: Schematic of Spinel structure.

Upon considering a single spinel unit, A-atoms tetrahedral site is shown in the middle surrounded by four oxygen atoms in a tetrahedral arrangement; on the other hand B-atoms octahedral sites are surrounded by six nearing oxygen atoms. Therefore, the big structure is

none other than the repetition of the mentioned configuration with eight „A" sites, sixteen „B"

sites, and thirty-two oxygen ions. In case of prospective chemical bonding, the voids in

between the oxygen ions play a crucial role whether to accommodate a bigger or smaller ion.

In the case of the metal ion being larger than the size of the intermolecular distance between

two oxygen ions it may not occupy to settle at the first place as oxygen ions are tightly and

closely packed together.

But in the contrast, the aforementioned metal ions who are bigger than the gap between two

oxygen ions can literally push them apart to make room for its own position. As a result,

these oxygen ions push the octahedral sites the same amount altering the sizes of tetrahedral

and octahedral sites [10, 11]. The oxygen ions connected with the octahedral sites move in

such a way as to shrink the size the octahedral cell by the same amount as the tetrahedral site

expands. The movement of the tetrahedral oxygen is reflected in a quantity called the oxygen

parameter, which is the distance between the oxygen ion and the face of the cube edge along

the cube diagonal of the spinel subcell [10].

Normal and Inverse spinels are resulted due to divalent metal ions on A-sights and B-sites

respectively. The basic magnetic properties of the ferrites are very sensitive functions of their

cation distributions. As a result, useful and interesting magnetic properties are prepared by

mixing two or more different types of metal ions. The individual preference of some ions for

certain sites resulting from their electronic configuration also play an important role. The

divalent ions are larger than the trivalent ions as more electrostatic attraction pull outer orbits

inward, where trivalent and divalent ions prefer to settle in tetrahedral and octahedral sites

respectively. There are also exceptions for some divalent ions preferring tetrahedral sites

instead of octahedral sites due to favorable electronic configuration. Therefore, these

preferences of the ions to accommodate into two possible lattice sites depends on ionic radii,

temperature, electrostatic energy of the lattice, electronic configuration of the surrounding anions, etc.

2.3 Magnetic Ordering

A material or the object subjected to an external magnetic field will experience torque that quantifies magnetic dipole moment having both magnitude and direction at the same time. The term „Magnetic Moment" is generally used instead of „magnetic field" in case of electron spin. For a current loop where the magnetic fields comply the right hand rule, the magnetic moment of the loop and the torque is given by μ and τ respectively [12]:

$$\mu = I\,(A) \times A(m^2) \quad \text{Where } \mu = \text{ Magnetic Moment} \quad (2.1)$$
$$I = \text{ Current}$$
$$A = \text{ Area enclosed by the current loop}$$

$$\tau = \mu \times B \text{ Where } \tau = \text{Torque} \quad (2.2)$$
$$B = \text{External Magnetic Field}$$
$$\mu = \text{ Magnetic Moment}$$

Equation 1 & 2: Magnetic moment & Torque

The figure below depicts the spin magnitudes of two electrons in two opposite directions creating magnetic fields very similar to the current loop referred earlier. For such conditions, the same magnitude will cancel out leaving zero magnetic fields which is very unlikely in the case of ferrimagnetic materials [12]. In fact ferrites have anti parallel magnetic moments of different magnitudes, giving rise to large magnetic moment in the presence of external magnetic field.
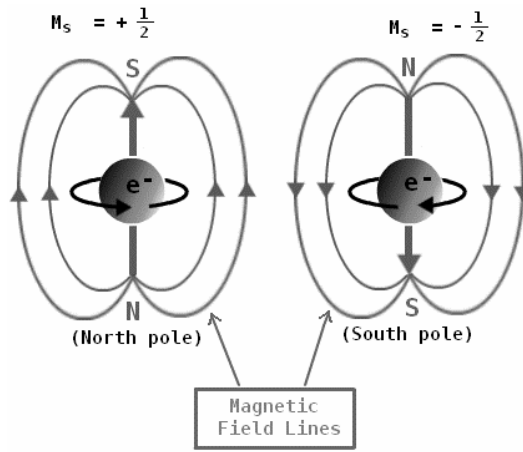
Figure 2.2: Magnetic Moment and Electron Spin.

Besides, for magnetic ordering to persist in solids, exchange interactions depending sensitively upon the inter-atomic distance and the nature of the chemical bonds (particularly of nearest neighbor atoms) should exist that couple them together. The magnetic ordering system becomes ferromagnetic below a certain temperature called the Curie temperature (T_C) during the dominance of positive exchange indicating parallel coupling of neighboring atomic moments to exist. On the contrary, anti-ferromagnetic characteristics are observed below a certain temperature, T_N, called the Néel temperature during the dominance of negative exchange implying coupling of neighboring atomic moments align anti-parallel to each other. Unequal strengths in opposite directions resulting into non-zero magnetization is nothing but the special case of anti-ferromagnetism, also known as ferrimagnetism. Moreover, due to long-range order and oscillatory nature of both positive and negative exchange interaction brought about by conduction electrons, complex structures like conical, helical or modified patterns might result. The temperature dependence of magnetic susceptibility can be classified as a useful property or a vital characterization parameter for magnetic materials. Ferrite materials do not obey the Curie-Weiss Law as the changes of inverse susceptibility with temperature of such material shows non-linear relationship [14, 19].

The Neél theory suggests that in ferrimagnetism, the interactions taken as effective are inter and intra-sublattice interactions A-B, A-A and B-B with the type of magnetic order depending on their relative strength. The idea of super exchange interaction was first proposed by Kramer and later developed by Anderson and Van Vleck [20, 21]. The sub lattice magnetizations will in general have different temperature dependences because the effective molecular fields acting on them are different. At a level, called the compensation point, sub lattice magnetization becomes equal meaning no magnetic moment. On the other hand, over the compensation point sub lattice magnetization does reverses direction and negative net magnetization takes place. Magnetic properties can be modified widely by cation substitution.

2.4. Domain Theory in Magnetism

The domain theory explains why Ferromagnets can retain their properties even after removing magnetic field. Ferromagnets are divided into some very small region that owns group electrons having the same direction within the same domain. These domains are about 10^{-12} to 10^{-8} m^3 in size. The interaction within one domain is so strong that they produce a net moment although it gets cancelled by the moment which is created by another domain. Ferromagnets contain millions of domain like these making the total magnetic flux zero. When a strong magnetic field is applied, the spin directions of all domain get aligned producing a humongous net magnetic flux that tries to keep the alignment same even after removing the field, however, the alignment may shift a little which is shown by the figure below. This result is explained by the hysteresis curve, why ferromagnets do not follow the same path of magnetization with increasing and decreasing of magnetic field which is known as the remnant magnetization.
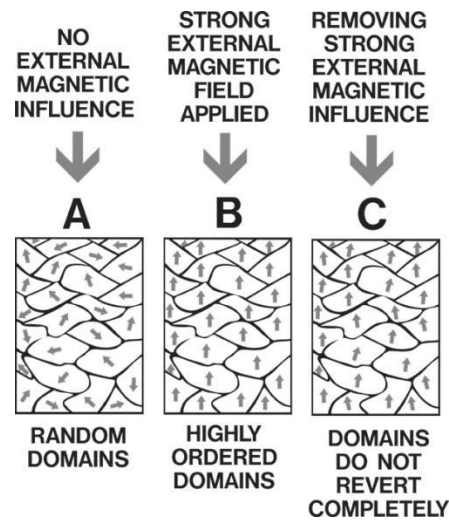
Figure 2.3: Domains in different field conditions.

2.5 Microstructures

In the simplest case, the grain boundary is the region, which accommodates the difference in crystallographic orientation between the neighboring grains. The ionic nature of ferrites leads to dislocation patterns considerably more complex than in metals, since electrostatic energy accounts for a significant fraction of the total boundary energy [14]. Besides, ceramic imperfections like pores, cracks, inclusions, residual strains can obstruct domain wall motion causing to reduce the magnetic property. Such obstruction can also act as energy wells that pin the domain wall and require higher activation energy to detach. Impurities or processing errors may also result microstructural imperfections like stresses.

Formation of exaggerated or discontinued grain growth explains intra-granular and inter-granular porosity. Such voids fractions are believed to result due to impurities in powder mixtures, different initial particle sizes, very high sintering temperature or low O_2 partial pressure in sintering chamber.

Porosity, a common term that appears with microstructure of crystallography, it is the void or empty space in a crystal structure. There are two types of porosity seen in grain size. a)

Intergranular and b) Intragranular porosity. Intragranular occurs within a grain and intergranular occurs in between grains.
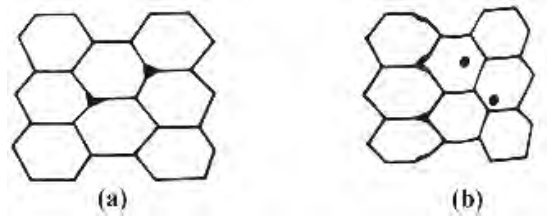
Figure 2.4: a) intergranular, b) intragranular porosity.

2.6 Theories of Permeability

Permeability is defined as the proportionality constant between the magnetic field induction B and applied field intensity H [14, 22, 23]:

$$B = \mu H \qquad (2.3)$$

If the applied field is very low, approaching zero, the ratio will be called the initial permeability is given by

$$\mu_i = \frac{\Delta B}{\Delta H}_{(\Delta H \to 0)} \qquad (2.4)$$

To conclude, permeability is simply the ability of a material to support magnetic fields within itself. The term was first coined in late 1800s by an English physicist Oliver Heaviside [22]. The relative increase or decrease in the resultant magnetic field inside a material compared with the magnetizing field in which the given material is located; or the property of a material that is equal to the magnetic flux density B established within the material by a magnetizing field divided by the magnetic field strength H of the magnetizing field. Magnetic permeability μ (Greek mu) is thus defined as $\mu = B/H$ in equation (2.4). Magnetic flux density

B is a measure of the actual magnetic field within a material considered as a concentration of magnetic field lines, or flux, per unit cross-sectional area. Magnetic field strength H is a measure of the magnetizing field produced by electric current flow in a coil of wire.

If a magnetic field is subjected to an AC magnetic material, we get

$$B = B_0 e^{i\omega t} \qquad (2.5)$$

It is observed that the magnetic flux density B experiences a delay which is caused due to the presence of various losses and is thus expressed as,

$$B = B_0 e^{i(\omega t-\delta)} \qquad (2.6)$$

Where, δ is the phase angle and indicates the delay of B with respect to H. The permeability is then given by

$$\mu = \frac{B}{H} = \frac{B_0 e^{i(\omega t-\delta)}}{H_0 e^{i\omega t}} = \frac{B_0 e^{-i\delta}}{H_0} = \frac{B_0}{H_0}\cos\delta - i\frac{B_0}{H_0}\sin\delta = \mu' - i\mu''$$

Where, $$\mu' = \frac{B_0}{H_0}\cos\delta \qquad (2.7)$$

and $$\mu'' = \frac{B_0}{H_0}\sin\delta \qquad (2.8)$$

The real part (μ') of the complex initial permeability represents the component of B that is in phase with H, so it corresponds to the normal permeability. If there are no losses we should get $\mu=\mu'$. The imaginary part (μ'') is the component that lags behind H by the phase angle. The presence of such a component requires supply of energy to maintain the alternating magnetization, regardless of the origin of delay. It is useful to introduce the loss factor $\tan\delta$ the ratio of μ'' to μ' which can be obtained by,

$$\frac{\mu^{//}}{\mu^{/}} = \frac{\dfrac{B_0}{H_0}\sin\delta}{\dfrac{B_0}{H_0}\cos\delta} = \tan\delta \qquad (2.9)$$

This $\tan\delta$ is called loss factor.

The quality factor is defined as the reciprocal of this loss factor, i.e.

$$\text{Quality factor} = \frac{1}{\tan\delta} \qquad (2.10)$$

And the relative quality factor,

$$Q = \frac{\mu^{/}}{\tan\delta} \qquad (2.11)$$
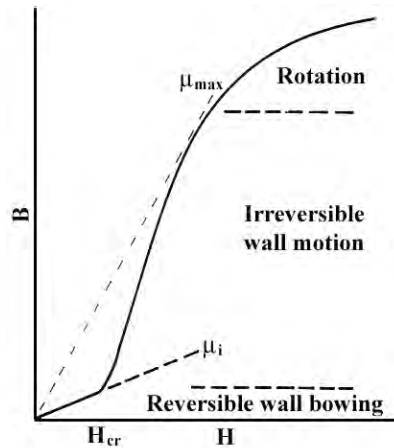
Figure 2.5: Schematic magnetization curve showing the important parameter: initial permeability, μ_i (the slope of the curve at low fields) and the main magnetization mechanism in each magnetization range.

The graph illustrates the behavior of both $\mu^{/}$ and $\mu^{//}$ with frequency are called the complex permeability spectrum of the material [31].The measurement of complex permeability gives us valuable information about the nature of domain wall and their movements. In dynamic measurements the eddy current loss is very important that occurs due to the irreversible domain wall

movements. The permeability of a ferrimagnetic substance is the combined effect of the wall permeability and rotational permeability mechanisms.

2.7. Mechanism of Permeability

The mechanisms can be explained as follows: A demagnetized magnetic material is divided into number of Weiss domains separated by Bloch walls. In each domain all the magnetic moments are oriented in parallel and the magnetization has its saturation value M_s. In the walls the magnetization direction changes gradually from the direction of magnetization in one domain to that in the next. The equilibrium positions of the walls result from the interactions with the magnetization in neighboring domains and from the influence of pores; crystal boundaries and chemical in homogeneities which tend to favor certain wall positions.

2.7.1 Wall Permeability

The mechanism of wall permeability arises from the displacementof the domain walls in small fields. Let us consider a piece of material in the demagnetized state, divided into Weiss domains with equal thickness L by means of 180° Bloch walls as shown in figure 2 (i). The walls are parallel to the YZ plane. The magnetization M_s in the domains is oriented alternately in the $+Z$ or $-Z$ direction. When a field H with a component in the $+Z$ direction is applied, the magnetization in this direction will be favored. A displacement dx of thewalls in the direction shown by the dotted lines will decrease the energy density by an amount [24, 25]:

$$\frac{2M_s H_z dx}{L} \quad (2.12)$$

This can be described as a pressure $M_s H_z$ exerted on each wall. The pressure will be counteracted by restoring forces which for small deviations may assume to be kdx per unit wall surface. The new equilibrium position is then given by

$$d = \frac{M_s H_z dx}{L} \quad (2.13)$$

From the change in the magnetization

$$\Delta M = \frac{2M_s d}{L}, \qquad (2.14)$$

The wall susceptibility χ_w may be calculated. Let H makes the angle θ with Z direction. The magnetization in the θ direction becomes

$$(\Delta M)_\theta = \frac{2M_s d}{L}\cos\theta, \text{ And with } H_z = H\cos\theta \text{ and } d = \frac{2M_s H_z}{K}$$

We obtain

$$\chi_w = \frac{(\Delta M)_\theta}{H} = \frac{4M_s^2 \cos^2\theta}{KL} \qquad (2.15)$$
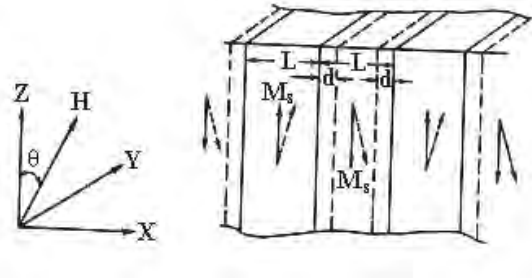
Figure 2.6: Magnetization by wall motion and spin rotation.

2.8 Rotational Permeability

The rotational permeability mechanism arises from rotation of the magnetization in each domain. The direction of M can be found by minimizing the magnetic energy E as a function of the orientation. Major contribution to E comes from the crystal anisotropy energy. Other contributions may be due to the stress and shape anisotropy. The stress may influence the magnetic energy via the magnetostriction. The shape anisotropy is caused by the boundaries of the sample as well as by pores, nonmagnetic inclusions and inhomogeneities. For small angular deviations, α_x and α_y may be written as

24

$$\alpha_x = \frac{M_x}{M_s} \text{ and } \alpha_y = \frac{M_y}{M_s}. \quad (2.16)$$

For equilibrium Z-direction E may be expressed as [26, 27]

$$E = E_0 + \frac{1}{2}\alpha_x^2 E_{xx} + \frac{1}{2}\alpha_y^2 E_{yy} \quad (2.17)$$

Where it is assumed that x and y are the principal axes of the energy minimum. Instead of E_{xx} & E_{yy}, the anisotropy field H_x^A and H_y^A are often introduced. Their magnitude is given by

$$H_x^A = \frac{E_{xx}}{2M_s} \text{ and } H_y^A = \frac{E_{yy}}{2M_s}, \quad (2.18)$$

H_x^A & H_y^A represent the stiffness with which the magnetization is bound to the equilibrium direction for deviations in x and y direction, respectively. The rotational susceptibilities $\chi_{r,x}$ and $\chi_{r,y}$ for fields applied along x and y directions, respectively are

$$\chi_{r,x} = \frac{M_s}{H_x^A} \text{ and } \chi_{r,y} = \frac{M_s}{H_y^A}. \quad (2.19)$$

For cubic materials it is often found that H_x^A and H_y^A are equal. For $H_x^A = H_y^A = H^A$ and a field H which makes an angle θ with the Z direction (as shown in Fig. 2.16) the rotational susceptibility, $\chi_{r,c}$ in one crystallite becomes

$$\chi_{r,c} = \frac{M_s}{H^A}\sin^2\theta \quad (2.20)$$

A polycrystalline material consisting of a large number of randomly oriented grains of different shapes, with each grain divided into domains in a certain way. The rotational susceptibility χ_r of the material has to be obtained as a weighted average of $\chi_{r,c}$ of each crystallite, where the mutual influence of neighboring crystallites has to be taken into account. If the crystal anisotropy dominates

other anisotropies, then H^A will be constant throughout the material, so only the factor $\sin^2 \theta$ (equation 2.17) has to be averaged. Snoek [27] assuming a linear averaging of $\chi_{r,c}$ and found

$$\chi_r = \frac{2M_s}{3H^A} \quad (2.21)$$

The total internal susceptibility

$$\chi = \chi_w + \chi_r = \frac{4M_s^2 \cos^2 \theta}{KL} + \frac{2M_s}{3H^A} \quad (2.22)$$

If the shape and stress anisotropies cannot be neglected, H^A will be larger. Any estimate of χ_r will then be rather uncertain as long as the domain structure, and the pore distribution in the material are not known. A similar estimate of χ_w would require knowledge of the stiffness parameter k and the domain width L. These parameters are influenced by such factors as imperfection, porosity and crystallite shape and distribution which are essentially unknown.

CHAPTER 3

Sample Preparation and Experimental Techniques

This chapter provides an overview of the sample preparation and methods that have been used to determine different parameters of the ferrites.

3.1 Chemical Compositions of Studied Samples

In this present work, the samples of Mn^{2+} doped Ni-Cu-Zn ferrite are synthesized and investigated. The samples are:

$(Ni_{0.4}Cu_{0.15}Zn_{0.45})_{1-x}Mn_xFe_2O_4$ (with x=0.30, 0.45)
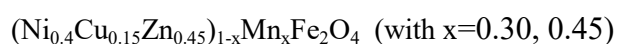
3.2 Various Methods for Preparing Samples

There are a number of methods which are followed to study ferrites and their compositions. Among these, the conventional ceramic process and solid state reaction method are widely used to prepare ferrite powder. Other methods are [8, 14],

1) Sol-gel synthesis

2) Co-precipitation

3) Organic precursors

4) Freeze dying

5) Spray dying

6) Combustion synthesis

7) Glass crystallization

For this experiment, solid state method reaction method is used which is described thoroughly below

3.2.1 Solid State Reaction Method

Solid state reaction method consists of several steps to get the final products which are been studied. Solids do not react at room temperature over normal time scales for which it is necessary to heat them at higher temperature to complete chemical reaction. This reaction depends on factors such as structural properties of the reactants, surface area of the solids, reactions conditions and their thermodynamics [8].

The required composition is usually prepared from the appropriate amount of raw materials of oxides or carbonates by crushing, grinding and milling.

Once the powders are finely ground, they are calcined in air for 5 hours at temperature above 500^0C. Calcine temperature may vary according to needs. The calcination process makes the impurities go away. The calcined powders are then again hand milled to ensure they are properly smoothed. The necessary pellets and toroid samples are prepared from the calcined powder according to the need using die punch assembly or hydrostatic or isostatic pressure. Sintering is carried out at temperatures from 900^0C to 1600^0C for a typical time of 1 to 10 hours in different atmospheres [28,29].

The general solid state reaction leading to a ferrite $MeFe_2O_4$ may be represented as

$$MeO+Fe_2O \xrightarrow{\text{Heat treatment}} MeFe_2O_4$$
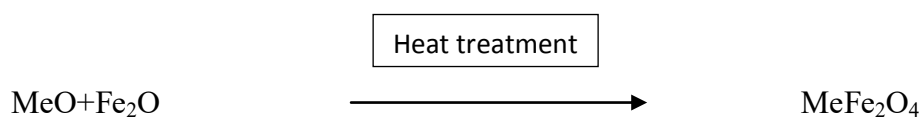
Where Me is the metal ions. There are basically four steps in the preparation of ferrites.

1) Preparation of materials to form an intimate mixture with the metal ions in the ratio which they will have in the final product.

2) Calcining the mixture to form ferrite.

3) Grinding the calcined powders and pressing to get the required shape.

4) Sintering to produce highly densified product.

Below is given the process of sample preparation through by a flowchart.

```
┌─────────────────────┐
│   Raw materials     │
└─────────────────────┘
           ⇓
┌─────────────────────┐
│   Weighing by       │
│   different mole    │
└─────────────────────┘
           ⇓
┌─────────────────────┐
│   Hand milling      │
└─────────────────────┘
           ⇓
┌─────────────────────┐
│   Calcination       │
└─────────────────────┘
           ⇓
┌─────────────────────┐
│   Hand milling      │
└─────────────────────┘
           ⇓
┌─────────────────────┐
│   Pressing to desired │
│   shapes            │
└─────────────────────┘
           ⇓
┌─────────────────────┐
│   Finished products │
└─────────────────────┘
```
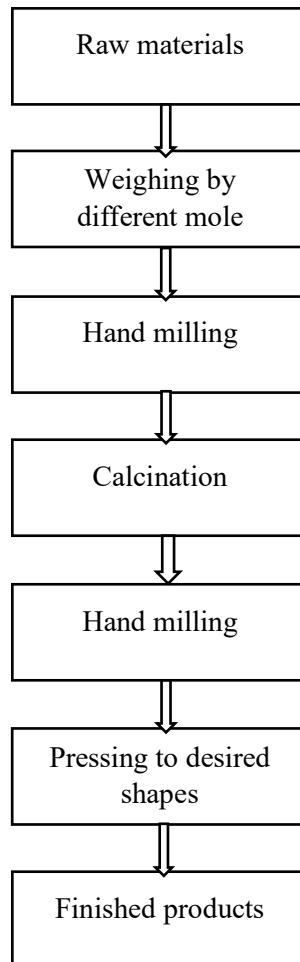
Figure 3.1: Flow chart of the stages in preparation of spinel ferrite.

3.2.2 Details of Calcination, Pressing and Sintering

Calcination is a process of obtaining a homogenous and phase pure composition of mixed powders by heating them for a certain amount of time at a certain temperature and then cooled down slowly. Calcination can be repeated several times to obtain a high degree of homogeneity. The calcined powders are then again crushed.

A binder is usually added prior to compaction at a concentration lower than 5wt%. Binders are polymers or waxes that is used to facilitate the particles flow during compacting and increase the bonding between particles. The most commonly used binder for ferrites is polyvinyl acid. During sintering binders decompose and are eliminated from the ferrite. Pressures are used to for compacting very widely but are commonly several tons per square inch. (i.e. up to $10^8 nm-2$) to desired toroid and pellet shapes.

Sintering process makes a sample more dense, tough body by heating a compacted powder for a certain period of time at high temperature enough to promote diffusion but surely below the melting point of the main component. The purposes of sintering process are-

1) To bind the particles to impart sufficient strength to the product.

2) To densify the material and eliminating pores.

3) Gain homogeneity by completing the reactions left unfinished in calcination.

Coble and burke [33] found out the empirical relation regarding rate of grain growth which is given by

$$\bar{d}=kt^n$$

Where $\bar{d}$ is the mean grain diameter. n is about 1/3, t is the sintering time and k is a temperature dependent parameter. Sintering is divide into 3 stages [14, 30]-

1) Contact area between particle increases.

2) Porosity changes from open to close porosity

3) Pore volume decreases and gains grow.

The following figure shows the grain growth at different sintering stages.
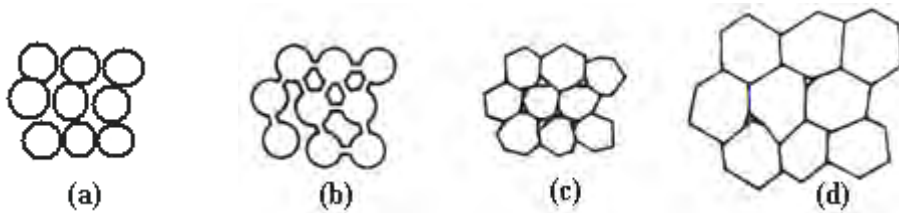
Figure 3.2: Schematic representation of sintering stages: (a) green body, (b) initial stage, (c)

intermediate stage, and (d) final stage.

3.2.3Stoichiometric Ratio Calculation

The following tables show the calculation of different amount of raw materials that was taken

to make the samples. For the samples used in this work, each was of a total of 15 grams and each

pellet and ring were made of 1 gram.

Table 1.0: atomic mass of the compounds.

Raw materials	Ni (g/mole)	Cu (g/mole)	Zn (g/mole)	Mn (g/mole)	C (g/mole)	Fe (g/mole)	O (g/mole)	Total (g/mole)
NiO	58.6934						15.9994	74.6928
Cu_2O		63.546					15.9994	143.0914
ZnO			65.38				15.9994	81.3794

$MnCO_3$				54.938	12.0107		15.9994	114.9469	
Fe_2O_3						55.845	15.9994	159.6882	

Table 1.1: total molecular mass of the sample.

X	Composition	Mass of the sample (g/mole)
0.30	$Ni_{0.28}Cu_{0.105}Zn_{0.315}Mn_{0.3}Fe_2O_4$	$(58.6934*0.28) +(63.546*0.105) +(65.38*0.315) + (54.938*0.3)$ $(55.845*2)+(15.9994*4)=235.87018$
0.45	$Ni_{0.22}Cu_{0.0825}Zn_{0.2475}Mn_{0.45}Fe_2O_4$	$58.6934*0.22+63.546*0.0825+65.38*0.2475+54.938*0.45+55.84*2+15.9994*4=234.746343$

Table 1.2: Calculation for the need of raw materials.

Composition	Need of	Amount (g/mole)
$Ni_{0.28}Cu_{0.105}Zn_{0.315}Mn_{0.3}Fe_2O_4$	NiO	$74.6928*0.4*15/238.11786$ $=1.8821$
	Cu_2O	$143.0914*0.15*15/238.11786$ $=1.3521$
	ZnO	$81.3794*0.45*15/238.11786$ $=2.3069$
	$MnCO_3$	0

	Fe$_2$O$_3$	159.6882*15/238.11786 =10.0594
Ni$_{0.22}$Cu$_{0.0825}$Zn$_{0.2475}$Mn$_{0.45}$Fe$_2$O$_4$	NiO	74.6928*0.22*15/234.746343 =1.0500
	Cu$_2$O	143.0914*0.0825*15/234.746343 =0.7543
	ZnO	81.3794*0.2475*15/234.746343 =1.28720
	MnCO$_3$	114.9469*0.45*15/234.746343 =3.3052
	Fe$_2$O$_3$	159.6882*15/234. 746343 =10.2039

3.2.4 Preparation of the Sample

Nano crystalline (Ni$_{0.4}$Cu$_{0.15}$Zn$_{0.45}$)$_{1-x}$Mn$_x$Fe$_2$O$_4$ (with x=0.00, 0.45) were prepared by solid state reaction method with the stoichiometric amount of raw materials. The pure grade powder (99.99% pure) of NiO, Cu$_2$O, ZnO, MnCO$_3$, Fe$_2$O$_3$ are weighted according to the required composition and hand milled for about 5 hours for chemical reaction to happen using an agitate mortar and pistol. Before using mortar and pistol, they were cleaned each and every time very carefully to avoid impurity mixing. This is facilitated further by calcination which is undertaken for 5 hours in air at a temperature of 950^{0}C. The calcined powders were granulated using polyvinyl acid a binder and pressed in to desired toroid and pellet shapes. In the final stage they were sintered at various temperatures from 1050^{0}C to 1200^{0}C in air for 5 hours. The temperature ramps for sintering are 5^{0}C /min for heating and 10^{0}C /min for cooling.

3.3 Experimental Techniques

In this chapter, the basic experimental techniques of measuring lattice parameter and frequency depended permeability of ferrite sample is described.

3.3.1 X-ray Diffraction

If a monochromatic radiation of wavelength λ is incident on periodic crystal plane at an angle of $\square$ and is diffracted at the same angle as shown in the figure, the Bragg diffraction condition in given by

$$2d\,Sin\,\theta = n\lambda \,(3.1)$$

Where d is the distance between crystal planes and n is the positive integer which represents the order of reflection. Equation (4.1) is known as Bragg law. This Bragg law suggests that the diffraction is only possible when $\lambda \leq 2d$ [36]. The X-ray diffraction provides substantial information of the crystal structure.

Pellets of $(Ni_{0.4}Cu_{0.15}Zn_{0.45})_{1-x}Mn_xFe_2O_4$ (with x=0.00, 0.45) sintered at 1100 is used for X-ray diffraction. The lattice parameter for each peak of each sample is calculated by the formula given below,

$$a = d\sqrt{h^2 + k^2 + l^2} \,(3.2)$$

Where h, k and l are the indices of the crystal planes. To determine the exact lattice parameter for each sample, Nelson-Riley method was used. The Nelson-Riley function $F\,(\theta)$ is given as

$$F(\theta) = \frac{1}{2}\left[\left(Cos^2\theta \,/\, Sin\,\theta\right) + \left(Cos^2\theta \,/\, \theta\right)\right](3.3)$$

The values of all peaks is plotted against $F (\square)$ of a sample. Using least square fit method, the lattice parameter a_0 is determined. The point where the least square fit straight line cut the y-axis is the actual lattice parameter of the samples.

3.3.2 Bulk Density Measurements

The physical or bulk density of the samples were determined by the formula,

$$\rho_{B=} M/V \qquad (3.4)$$

Where ρ_B is the bulk density, M is the wright of the sample and V is the volume. V was determined by calculating the radius and thickness of the pellet and then put into the formula,

$$V=\pi r^2 h$$

The theoretical density is calculated by using the following expression

$$\rho_{th} = \frac{8M}{N_A a_o^3} g/cm^3 \qquad (3.5)$$

Where n is the Avogadro number (6.02×10^{23} mol^{-1}), m is the molecular weight. Porosity was calculated from the relation,

$$\{100(\rho_{th} - \rho_B)/\rho_{th}\}\% \qquad (3.6)$$

3.3.3 Study of Microstructure

Microstructure of the ferrite composition shows the grain size of the sample which is sintered at 1100^0C.The samples were observed under high resolution optical microscope and photographed. Grain diameters were determined by liner intercept technique for which several random horizontal and vertical lines were drawn on the micrographs. Therefore the

number of grains were counted that intersected and measured the length of the grains along the line traversed. Finally the grain size was calculated.

3.3.4 Complex Permeability Measurement

Permeability is a quantity that defines the change in self-inductance of a coil in the presence of a magnetic core. The core is taken as a toroid shape to avoid demagnetizing effects.

Complex initial permeability is given by

$$Z = R + jX = j\omega L_0 \mu = j\omega L_0 (\mu' - j\mu'') \quad (3.7)$$

Where the resistive part is,

$$R = \omega L_0 \mu'' \quad (3.8)$$

And the reactive part is,

$$X = \omega L_0 \mu' \quad (3.9)$$

Here, L_0 is the inductance of the winding coil in air that is without loss.

μ is the permeability of the magnetic core

On the above expressions, the real part and the imaginary part were calculated by $\mu_i' = L_s/L_0$ and $\mu_i'' = \mu_i' \tan\delta$, where L_s is the self-inductance of the sample core sample core and $L_0 = \mu_o N^2 S / \pi \overline{d}$ derived geometrically.

N is the number of turns of the coil ($N = 6$), S is the area of cross section of the toroidal sample as given below:

$$S = d \times h, \quad (3.10)$$

Where $\qquad d = \dfrac{d_2 - d_1}{2}$,

$d_1 = $ Inner diameter,

$d_2 = $ Outer diameter,

$h = $ Height

And $\bar{d}$ is the mean diameter of the toroidal sample as given below:

$$\bar{d} = \frac{d_1 + d_2}{2}$$

The relative quality factor is determined from the ratio $\dfrac{\mu_i^{/}}{\tan \delta}$. (3.10)

Chapter 4

Results and Discussion

4.1. X-Ray Diffraction Analysis

X-ray diffraction was done on $(Ni_{0.4}Cu_{0.15}Zn_{0.45})_{1-x}Mn_xFe_2O_4$ (with x=0.30, 0.45) that were sintered at 1100^0C in air for 5 hours to explore the spinel structure and physical properties of the samples. The results found in the experiment indicated that these materials have formed a well-defined single crystalline phase and formation of spinel structure for each composition. The positions of the peaks matched with the reported value. In figure 4.1, X-ray patterns are shown for different compositions.
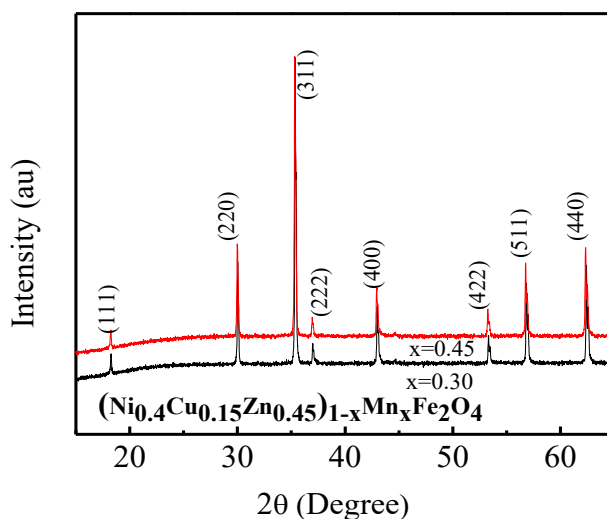
Figure 4.1: The X-ray diffraction patterns for Intensity $(Ni_{0.4}Cu_{0.15}Zn_{0.45})_{1-x}Mn_xFe_2O_4$ (with x=0.30, 0.45).

From the XRD report, lattice parameter is found with the help of Nelson-Riley function. In figure 4.2, the lattice parameter is shown as a function of Mn^{2+} content.
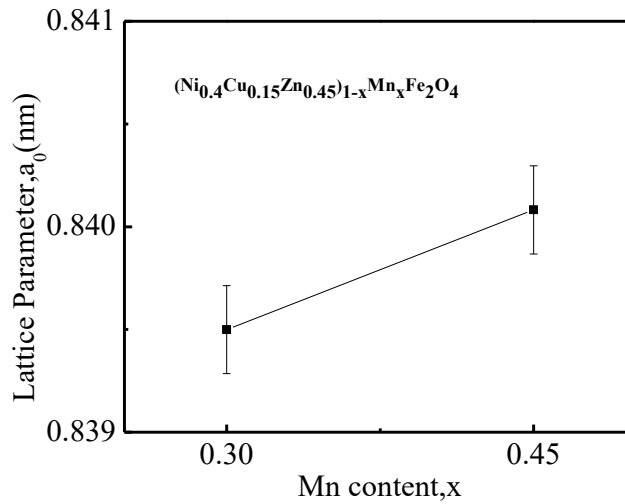
Figure 4.2: The variation of lattice parameter with Mn^{2+} for $(Ni_{0.4}Cu_{0.15}Zn_{0.45})_{1-x}Mn_xFe_2O_4$.

The parameter increases with Mn^{2+} content which can be explained in terms of ionic radii. Mn^{2+} has an ionic radius of 0.83 Å [] which replaces Zn^{2+} (0.74 Å), Ni^{2+} (0.69Å) and Cu^{2+} (0.72Å) []. This increment is because of the small cations are getting replaced by big cations for which the lattice parameter has increased with Mn^{2+} content.

4.2 Bulk Density and Porosity

Bulk density, theoretical density and porosity of various compositions of $(Ni_{0.4}Cu_{0.15}Zn_{0.45})_{1-x}Mn_xFe_2O_4$ (x=0.30, x=0.45) sintered at 1100, 1150 and 1200^0C have been calculated using the Eq-3.5, Eq-3.6, and Eq-3.7 respectively. The following figure 4.3 shows the variation of theoretical density and bulk density with increasing content of Mn^{2+} at sintering temperature of 1100^0C. The bulk density decreases with Mn^{2+} content which can be explained by the atomic weights of the elements of the ferrite composition. Mnhas the atomic weight of 54.938 (amu) [23] whereas Ni, Zn, Cu have 58.6934(amu), 65.38(amu), 63.546(amu) respectively [27]. With Mn^{2+} reducing the other cations, the total mass of the sample has also been reduced. As a result, the bulk density has decreased. Theoretical density depends on the lattice constant and molecular mass of the samples. It is evident that the theoretical densities

are larger on every point than their corresponding bulk densities which may be due to the pores in the samples. Another trend can be identified from the same graph which shows the theoretical density has also deceased although the lattice parameter (a_0) increased. This may be caused by Mn doping for which the total molecular mass lessened with increasing Mn content. Similar behavior is observed by Hamid [33].
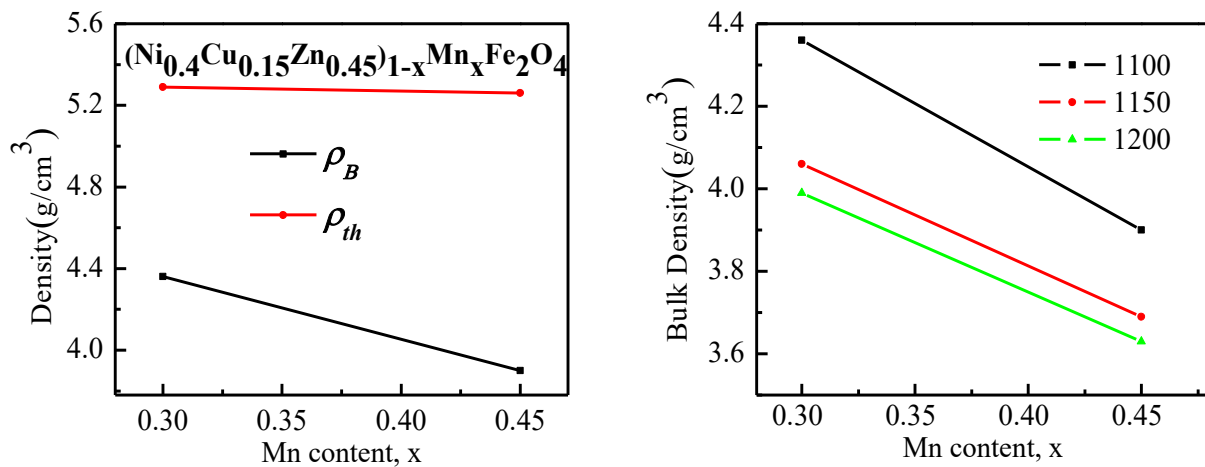
Fig 4.3: The variation of (a) bulk and theoretical density at 1100^0C and (b) Bulk density with Mn^{2+} content for various ferrites sintered at different sintering temperature for $(Ni_{0.4}Cu_{0.15}Zn_{0.45})_{1-x}Mn_xFe_2O_4$.

.
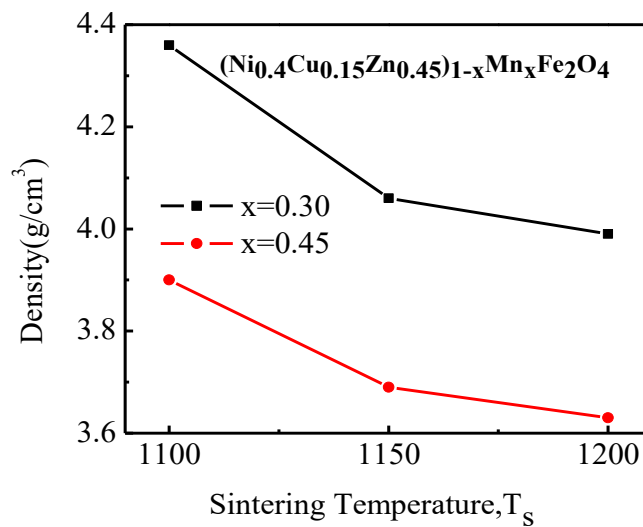
Figure 4.4: Bulk density for various $(Ni_{0.4}Cu_{0.15}Zn_{0.45})_{1-x}Mn_xFe_2O_4$ sintered at different temperatures T_s for $(Ni_{0.4}Cu_{0.15}Zn_{0.45})_{1-x}Mn_xFe_2O_4$.

In fig 4.4, it is seen that bulk density reduces with increasing temperature. Bulk density reduction with increasing sintering temperature may be explained with the help of intragranular porosity.
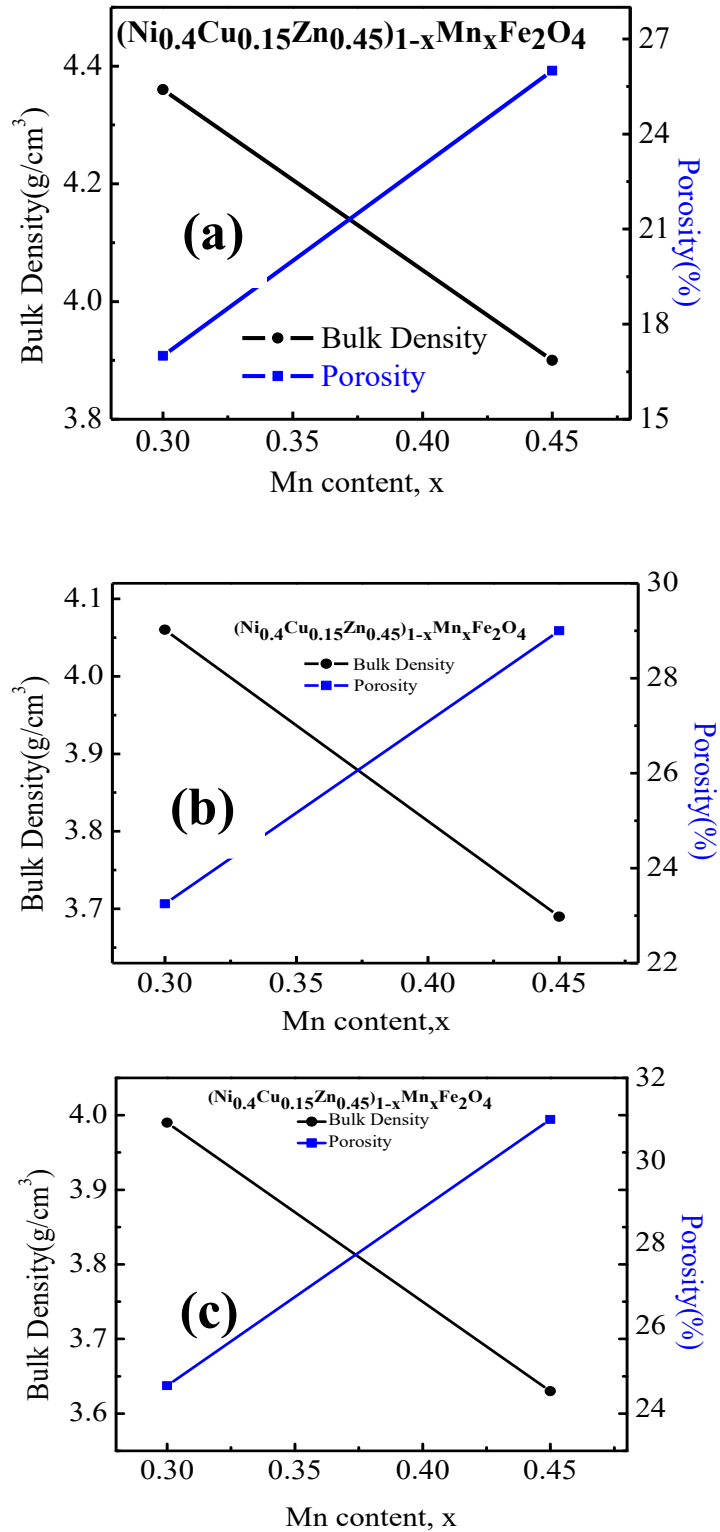
Fig 4.5: Bulk density and porosity with Mn content for $(Ni_{0.4}Cu_{0.15}Zn_{0.45})_{1-x}Mn_xFe_2O_4$ sintered at a) 1100 b) 1150 and c) 1200^0C.

The relation between bulk density and porosity for different sintering temperatures are shown in fig 4.5. At high temperature the intragranular porosity is increased due to discontinuous grain growth. It rises with temperature that makes grain growth faster which eventually leaves pores trapped inside grains. Hence, results in density reduction

4.3. Microstructural Investigation

The optical micrographs of various samples of $(Ni_{0.4}Cu_{0.15}Zn_{0.45})_{1-x}Mn_xFe_2O_4$ sintered at 1100^0C have also been observed. The following figures show the graphs of two different compositions that varies with x. The average grain size decreases with increase of Mn^{2+} that may be due to the modified chemical properties as a result of Mn^{2+} substitution. This decrease of grain size may also has resulted from the fact that each element has a different melting temperature. Mn has a melting temperature of 1518 K [36] which is lower than Ni (1726 K) but higher than Cu (1357 K) and Zn (692 K) [37, 42].

(a) x = 0.30   (b) x = 0.45
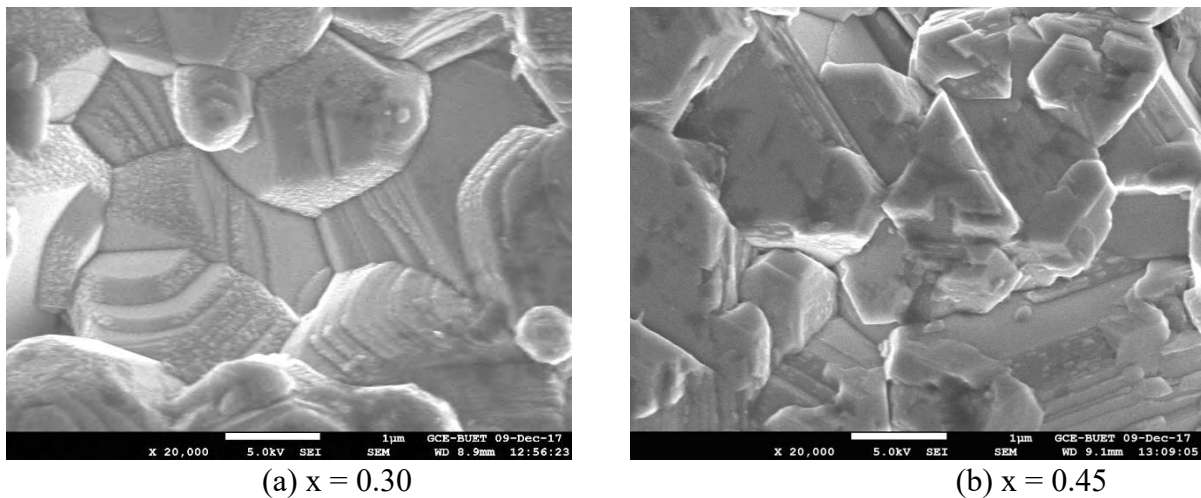
Fig 4.6: Micrographs of $(Ni_{0.4}Cu_{0.15}Zn_{0.45})_{1-x}Mn_xFe_2O_4$ sintered at 1100^0C

During the solidification process the melting point of different elements play a crucial role that cause each compositions to attain completely different physical and chemical properties. Another reason for grain size reduction can be the increasing amount of pores and voids within grains and grain boundaries.

Table 4.1: Lattice parameter, theoretical density, bulk density, porosity, natural resonance frequency, grain size of various $(Ni_{0.4}Cu_{0.15}Zn_{0.45})_{1-x}Mn_xFe_2O_4$ at different sintering temperatures.

x	$a_0(nm)$	$T_s(^0C)$	ρ_{th} (g/cm³)	ρ_B (g/cm³)	P (%)	f_r (MHz)	Grain size(μm)	$\mu_i^{/}$ (at 10⁵ Hz)
0.30	0.8394	1100	5.29	4.36	18	21.59	1.38	131
		1150		4.06	23	17.86		115
		1200		3.99	25	10.7		168
0.45	0.8400	1100	5.26	3.9	26	23.53	1.27	130
		1150		3.69	29	19.03		111
		1200		3.63	31	11.19		133

4.4. EDS

The purity and chemical composition of samples were checked using EDS analysis. Figure 4.7 and 4.8 show disparate surface points in EDS spectrum of the samples with x=0.30 and x=0.45 to conclude the homogeneity of the investigated samples.

The concentrations of different constituents involved in the investigated sample at 10 KeV over various points on the surface of $(Ni_{0.4}Cu_{0.15}Zn_{0.45})_{1-x}Mn_xFe_2O_4$ with increasing Mn content are given in table 4.2. This table indicates the concentrations of different constituents are close to each other. The spectrum images reveal no trace of impurity and molar proportions of the present elements are in good agreement with that of expected values which shows there is no chemical reaction or any loss of ingredients.

View000
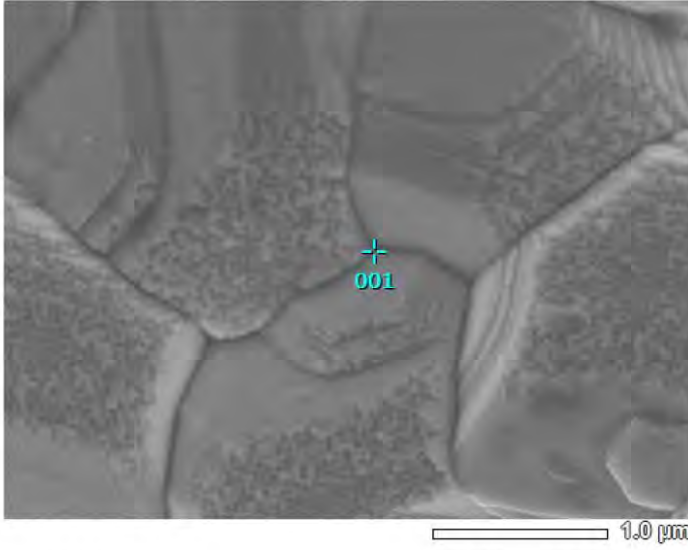
```
1.0 µm
```

```
Title       : IMG1
--------------------------
Instrument  : 7600F
Volt        : 5.00 kV
Mag.        : x 30,000
Date        : 2017/12/09
Pixel       : 512 x 384
```

001   VFS = 1552 count
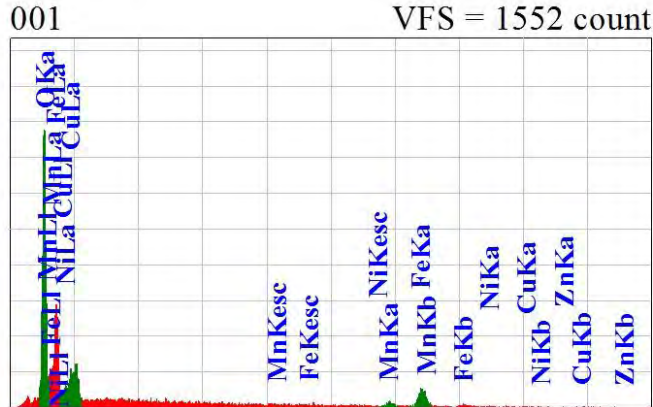

```
Acquisition Parameter
Instrument   : 7600F
Acc. Voltage : 10.0 kV
Probe Current: 1.00000 nA
PHA mode     : T3
Real Time    : 30.21 sec
Live Time    : 30.00 sec
Dead Time    : 0 %
Counting Rate: 838 cps
Energy Range :  0 - 20 ke\
```

```
ZAF Method Standardless Quantitative Analysis
Fitting Coefficient : 0.1072
Element    (keV)   Mass%  Sigma  Atom%  Compound  Mass%  Cation      K
 O K       0.525   31.82   0.34  62.73                           43.0790
Mn K       5.894    6.77   0.61   3.88                            6.6385
Fe K       6.398   38.22   1.57  21.58                           38.5714
Ni L       0.851   10.19   0.73   5.47                            4.1099
Cu L       0.930    4.37   0.25   2.17                            3.9353
Zn L       1.012    8.64   0.41   4.17                            3.6659
Total             100.00         100.00
```

POINT 1

View000

Title   : IMG1

Instrument : 7600F
Volt   : 5.00 kV
Mag.   : x 30,000
Date   : 2017/12/09
Pixel   : 512 x 384

1.0 μm

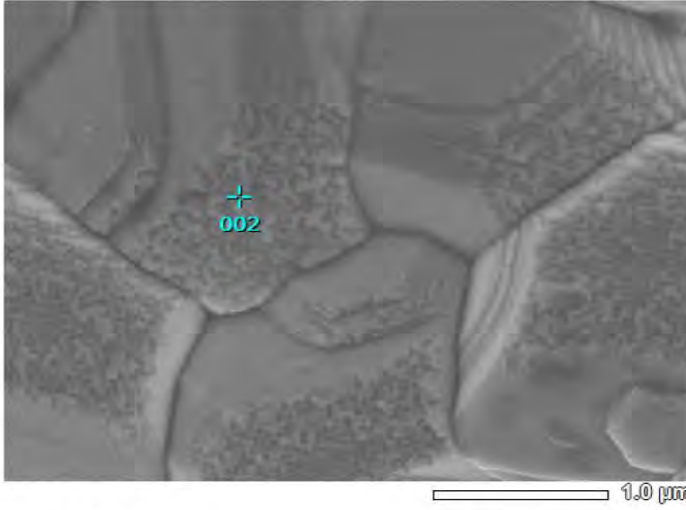002   VFS = 1769 count

Acquisition Parameter
Instrument   : 7600F
Acc. Voltage : 10.0 kV
Probe Current: 1.00000 nA
PHA mode   : T3
Real Time   : 30.26 sec
Live Time   : 30.00 sec
Dead Time   : 0 %
Counting Rate: 1025 cps
Energy Range : 0 - 20 keV

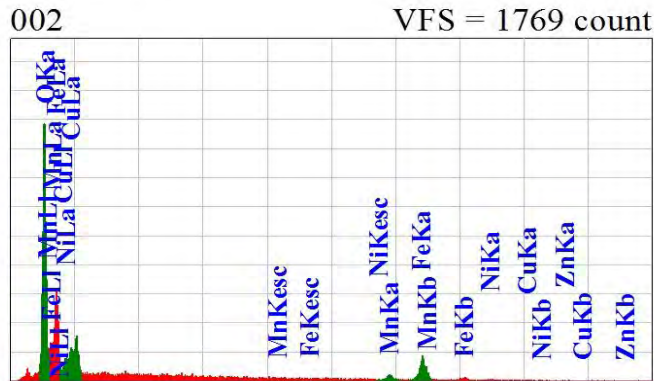ZAF Method Standardless Quantitative Analysis
Fitting Coefficient : 0.1130

Element	(keV)	Mass%	Sigma	Atom%	Compound	Mass%	Cation	K
O K	0.525	30.36	0.31	61.11				41.4697
Mn K	5.894	8.21	0.58	4.81				8.1743
Fe K	6.398	37.67	1.40	21.72				38.6102
Ni L	0.851	10.84	0.65	5.94				4.4412
Cu L	0.930	3.57	0.22	1.81				3.2683
Zn L	1.012	9.36	0.37	4.61				4.0362
Total		100.00		100.00				

JED-2300 AnalysisStation   JEOL

POINT 2

46

View000

```
Title        : IMG1
---------------------------
Instrument   : 7600F
Volt         : 5.00 kV
Mag.         : x 30,000
Date         : 2017/12/09
Pixel        : 512 x 384
```

1.0 μm

003   VFS = 1556 count
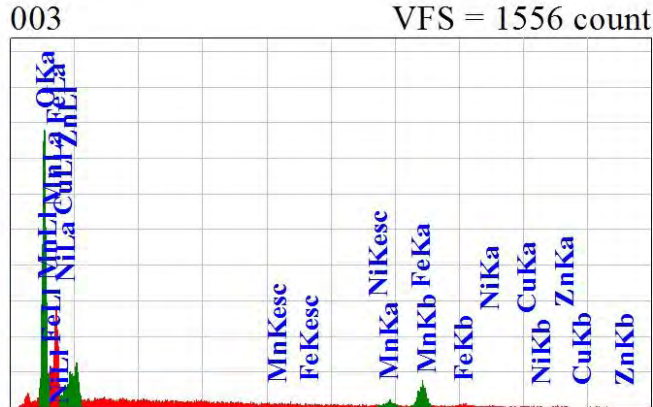
```
Acquisition Parameter
Instrument   : 7600F
Acc. Voltage : 10.0 kV
Probe Current: 1.00000 nA
PHA mode     : T3
Real Time    : 30.22 sec
Live Time    : 30.00 sec
Dead Time    : 0 %
Counting Rate: 928 cps
Energy Range :  0 - 20 ke\
```
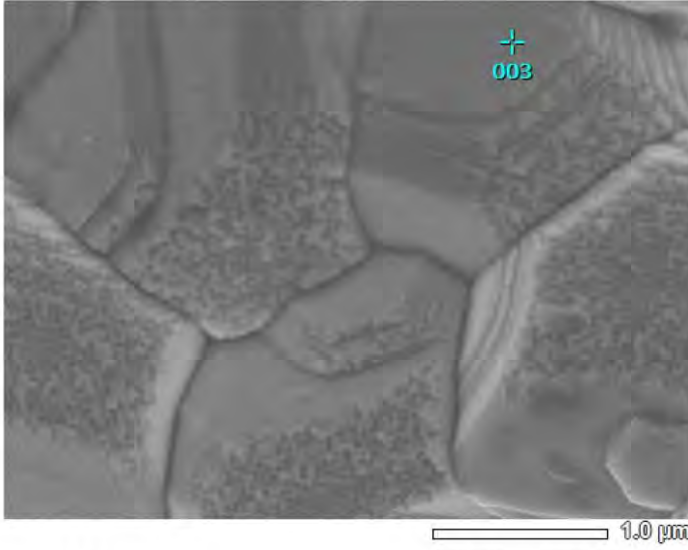
```
ZAF Method Standardless Quantitative Analysis
Fitting Coefficient : 0.1080
Element    (keV)    Mass%   Sigma   Atom%   Compound   Mass%   Cation        K
 O K       0.525    28.80   0.31    59.31                               39.3185
Mn K       5.894     5.60   0.55     3.36                                5.6082
Fe K       6.398    41.71   1.53    24.60                               43.0041
Ni L       0.851    10.99   0.67     6.17                                4.4860
Cu L       0.930     4.32   0.23     2.24                                3.9180
Zn L       1.012     8.58   0.37     4.33                                3.6653
Total              100.00          100.00
```

POINT 3

Fig 4.7 EDS patterns at different points for x=0.3.

View000

```
Title      : IMG1
--------------------------
Instrument : 7600F
Volt       : 5.00 kV
Mag.       : x 30,000
Date       : 2017/12/09
Pixel      : 512 x 384
```

1.0 μm

001   VFS = 1573 count
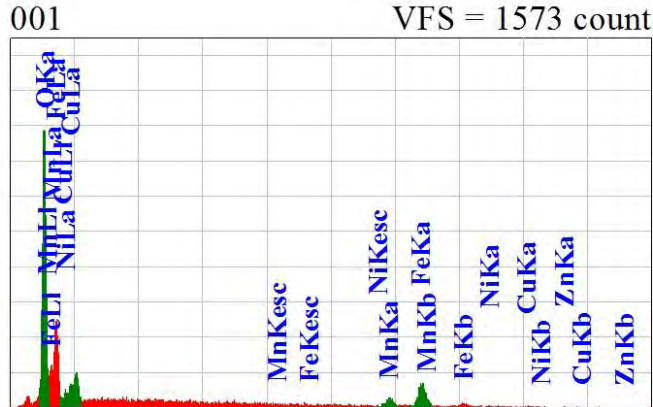
```
Acquisition Parameter
Instrument  : 7600F
Acc. Voltage : 10.0 kV
Probe Current: 1.00000 nA
PHA mode     : T3
Real Time    : 30.23 sec
Live Time    : 30.00 sec
Dead Time    : 0 %
Counting Rate: 862 cps
Energy Range :  0 - 20 ke\
```

```
ZAF Method Standardless Quantitative Analysis
Fitting Coefficient : 0.1043
Element     (keV)    Mass%   Sigma   Atom%  Compound  Mass%  Cation       K
 O K        0.525    29.02    0.31   59.33                            39.1666
Mn K        5.894    11.77    0.73    7.01                            11.3974
Fe K        6.398    41.48    1.55   24.30                            41.1182
Ni L        0.851     7.90    0.60    4.40                             2.9566
Cu L        0.930     2.75    0.20    1.42                             2.4111
Zn L        1.012     7.09    0.34    3.55                             2.9501
Total                100.00          100.00
```
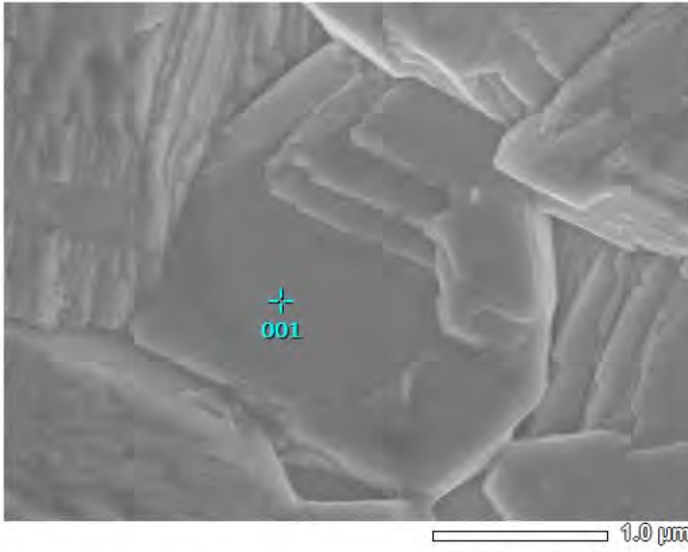
JED-2300 AnalysisStation   JEOL

POINT 1

View000

```
Title       : IMG1
---------------------------
Instrument  : 7600F
Volt        : 5.00 kV
Mag.        : x 30,000
Date        : 2017/12/09
Pixel       : 512 x 384
```

002   VFS = 1449 count


```
Acquisition Parameter
Instrument  : 7600F
Acc. Voltage : 10.0 kV
Probe Current: 1.00000 nA
PHA mode     : T3
Real Time    : 30.22 sec
Live Time    : 30.00 sec
Dead Time    : 0 %
Counting Rate: 834 cps
Energy Range :  0 - 20 ke\
```
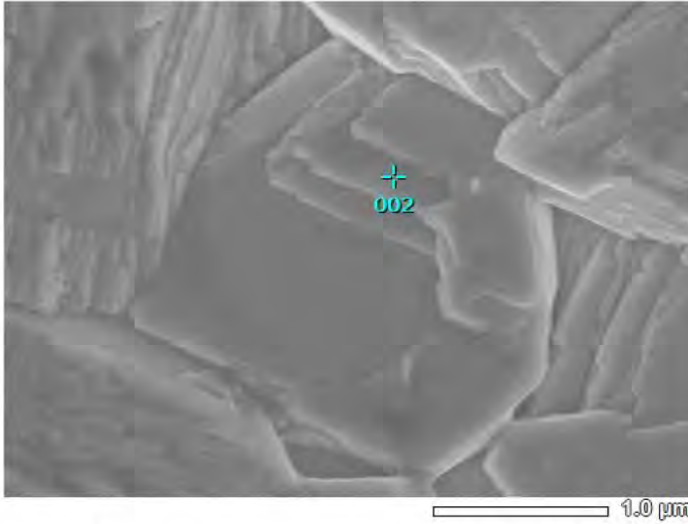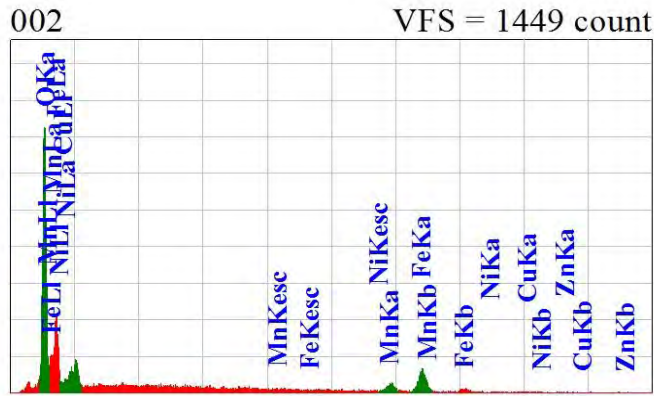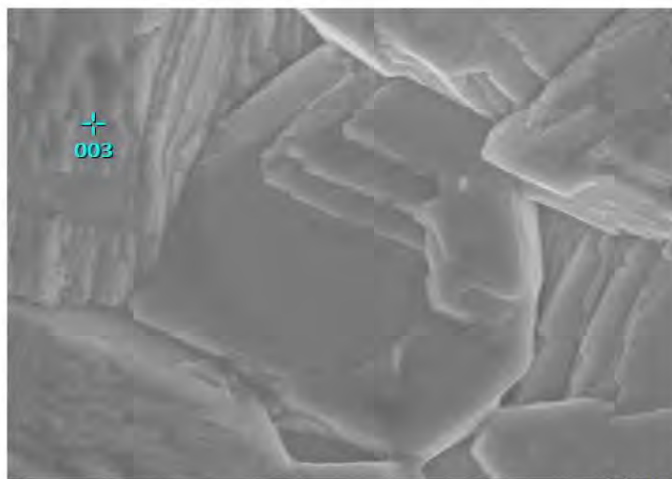
```
ZAF Method Standardless Quantitative Analysis
Fitting Coefficient : 0.1004
Element      (keV)   Mass%   Sigma   Atom%  Compound  Mass%  Cation        K
 O K        0.525   28.93    0.13    59.21                              38.6992
Mn K        5.894    9.74    0.47     5.81                               9.3155
Fe K        6.398   45.60    0.80    26.74                              44.4955
Ni L        0.851    5.77    0.53     3.22                               2.0868
Cu L        0.930    2.85    0.17     1.47                               2.4692
Zn L        1.012    7.11    0.26     3.56                               2.9339
Total              100.00          100.00
```
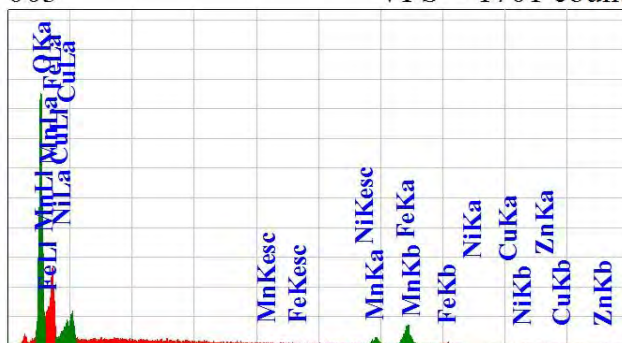
JED-2300 AnalysisStation   **JEOL**

POINT 2

49

View000

Title   : IMG1

Instrument : 7600F
Volt   : 5.00 kV
Mag.   : x 30,000
Date   : 2017/12/09
Pixel   : 512 x 384

1.0 μm

003   VFS = 1701 count

Acquisition Parameter
Instrument : 7600F
Acc. Voltage : 10.0 kV
Probe Current: 1.00000 nA
PHA mode   : T3
Real Time   : 30.23 sec
Live Time   : 30.00 sec
Dead Time   : 0 %
Counting Rate: 950 cps
Energy Range : 0 - 20 keV

ZAF Method Standardless Quantitative Analysis
Fitting Coefficient : 0.1061

Element	(keV)	Mass%	Sigma	Atom%	Compound	Mass%	Cation	K
O K	0.525	30.93	0.32	61.56				41.5532
Mn K	5.894	12.02	0.73	6.97				11.5259
Fe K	6.398	38.99	1.51	22.23				38.2312
Ni L	0.851	7.26	0.62	3.94				2.7236
Cu L	0.930	3.16	0.21	1.58				2.7760
Zn L	1.012	7.64	0.36	3.72				3.1900
Total		100.00		100.00				

JED-2300 AnalysisStation   JEOL

POINT 3

Figure 4.8: EDS Patterns at different points for x=0.45.

Table 4.2: Concentrations of different constituents.

Composition	Elements	Point1 (%)	Point2 (%)	Point3 (%)	Expected (%)
$Ni_{0.28}Cu_{0.105}Zn_{0.315}Mn_{0.3}Fe_2O_4$	Ni	10.19	10.84	10.99	6.96
	Cu	4.37	3.57	4.32	2.82
	Zn	8.64	9.36	8.58	8.73
	Mn	6.77	8.21	5.60	6.98
	Fe	38.22	37.67	41.71	47.35
	O	31.82	30.36	28.80	27.13
$Ni_{0.28}Cu_{0.105}Zn_{0.315}Mn_{0.45}Fe_2O_4$	Ni	7.90	5.77	7.26	5.50
	Cu	2.75	2.85	3.16	2.23
	Zn	7.09	7.11	7.64	6.89
	Mn	11.77	9.74	12.02	10.53
	Fe	41.48	45.60	38.99	47.57
	O	29.02	28.93	30.93	27.26

4.5. Complex Initial Permeability

The variation of complex permeability spectra for various samples of $(Ni_{0.4}Cu_{0.15}Zn_{0.45})_{1-x}Mn_xFe_2O_4$ sintered at 1100, 1150 and 1200^0C have been depicted in the figures 4.9,4.10and 4.11 respectively. The initial permeability $(\mu_i^{/})$ decreases with increasing Mn^{2+} content which is shown in figure 4.9. The general characteristic spectra of the real part remain constant in a certain frequency range, but then drop sharply at higher frequencies to a very small value.

The decrease in permeability with increasing Mn^{2+} can be explained as the grain size has decreased. Permeability is greatly dependent on the internal structure of the composition on how the grain has grown, what kind porosity has been produced within the samples. The more Mn is added to the compositions, the grain size decreased which eventually resulted in lowering the permeability. The imaginary part $(\mu_i^{//})$ of the permeability spectra also have decreased with values of x.

The relative quality factor for various samples of $(Ni_{0.4}Cu_{0.15}Zn_{0.45})_{1-x}Mn_xFe_2O_4$ have been calculated from the loss factor for different sintering temperatures. This Q-factor is important for practical applications that indicate the measure of performance. Figure 4.10 shows the relative quality factor with increasing Mn^{2+} content for 1100, 1150 and 1200^0C sintering temperatures. In figure 4.11, permeability and relative quality factor for different values of x with varying temperature is given. It is noticed that RQF is high for $(Ni_{0.4}Cu_{0.15}Zn_{0.45})_{1-x}Mn_xFe_2O_4$ when x=0.30 at 1200^0C. At higher frequency, a sudden increase in permeability is noticed after a continuation of stability. This frequency is known as natural resonance frequency beyond which the permeability takes a sharp fall. This is common for all the values of x in every temperature.
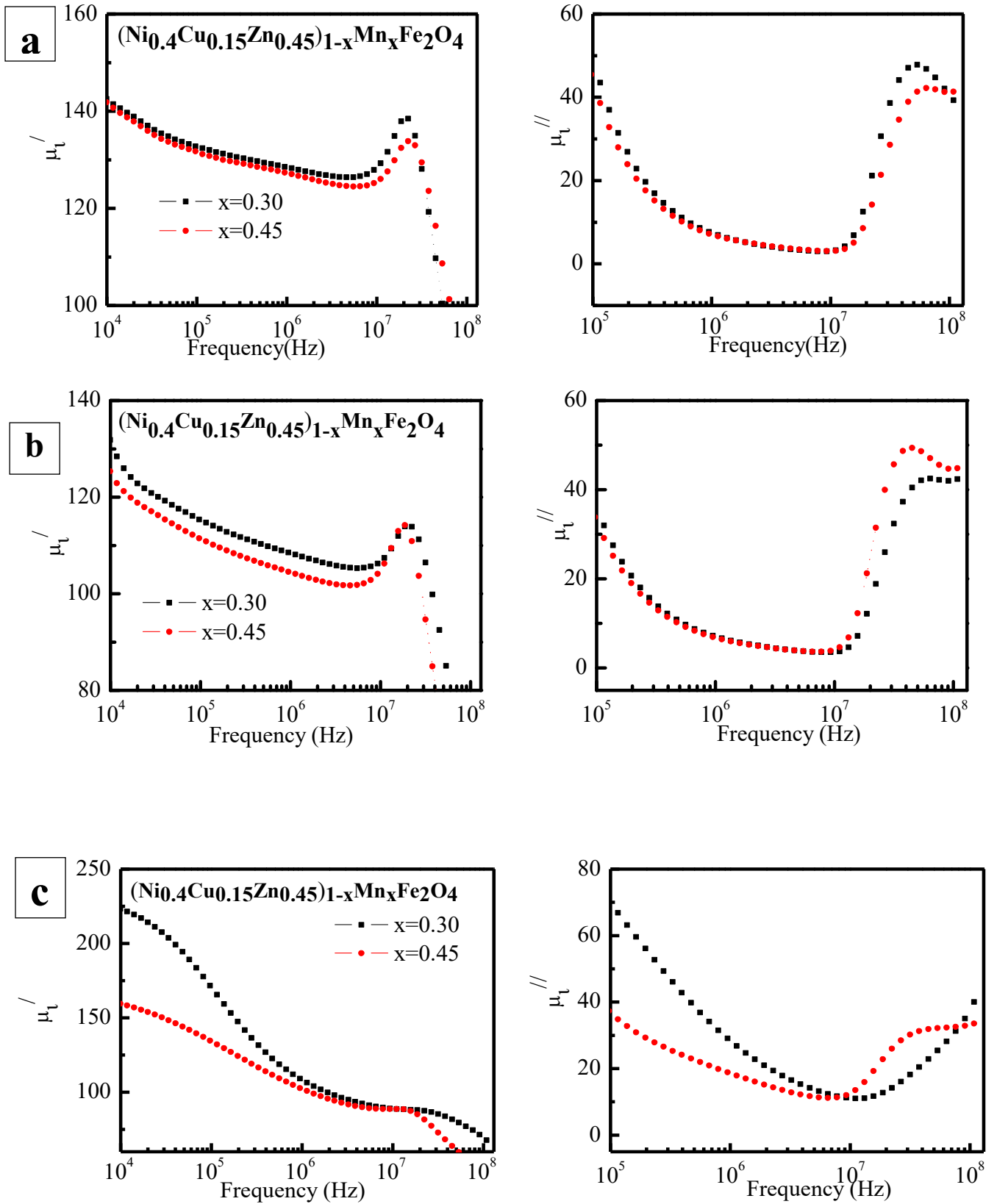
Figure 4.9: The real and imaginary part of permeability spectrum for $(Ni_{0.4}Cu_{0.15}Zn_{0.45})_{1-x}Mn_xFe_2O_4$ sintered at
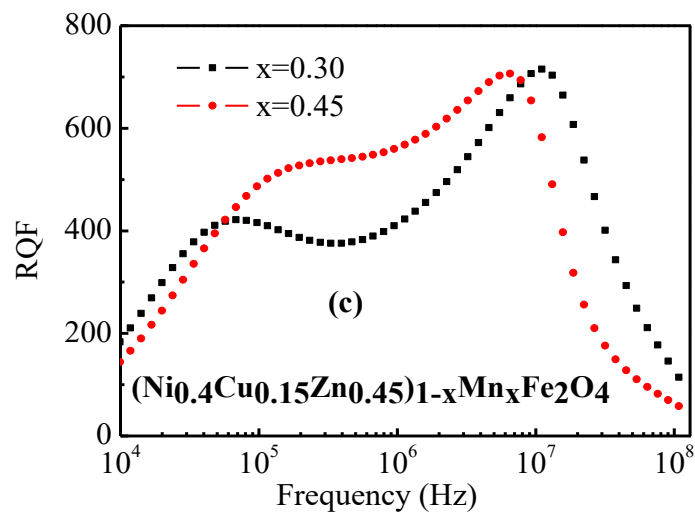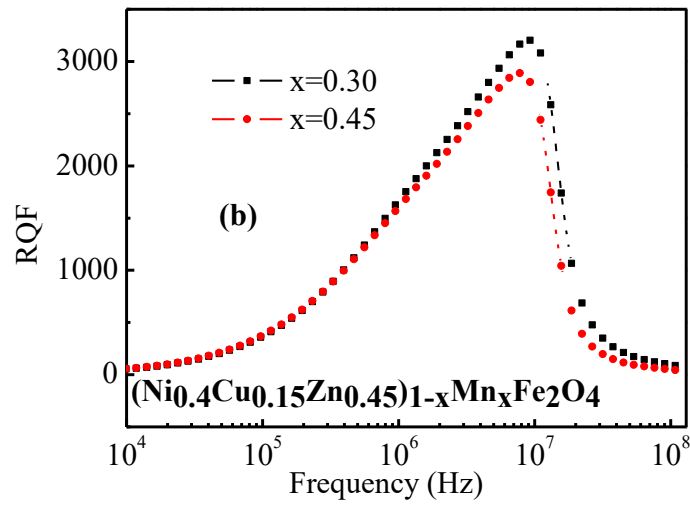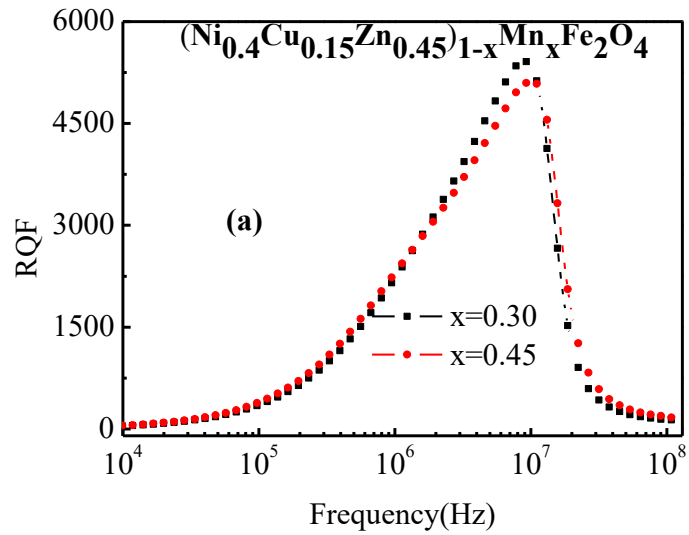
(a) 1100 (b) 1150 and (c) 1200^0C in air.

Figure 4.10: Relative quality factor (RQF) of permeability spectrum for $(Ni_{0.4}Cu_{0.15}Zn_{0.45})_{1-x}Mn_xFe_2O_4$ sintered

at (a) 1100 (b) 1150 and (c) 1200^0C in air.

The decrease in permeability with increasing sintering temperature given in fig 4.11 can be explained in terms of porosity and density. As seen from fig 4.5 the bulk density decreases and also the porosity increases when the sintering temperature rises. Pores affect the moments of domains that tend to align along the direction of applied magnetic field. It is found that bulk density of the sample is a linear function of grain size. The $\mu_i^/$ is dependent on both the domain wall susceptibility and intrinsic rotational susceptibility. The domain wall susceptibility is affected by the grain size. As the grain size decreases, the permeability also falls with it.
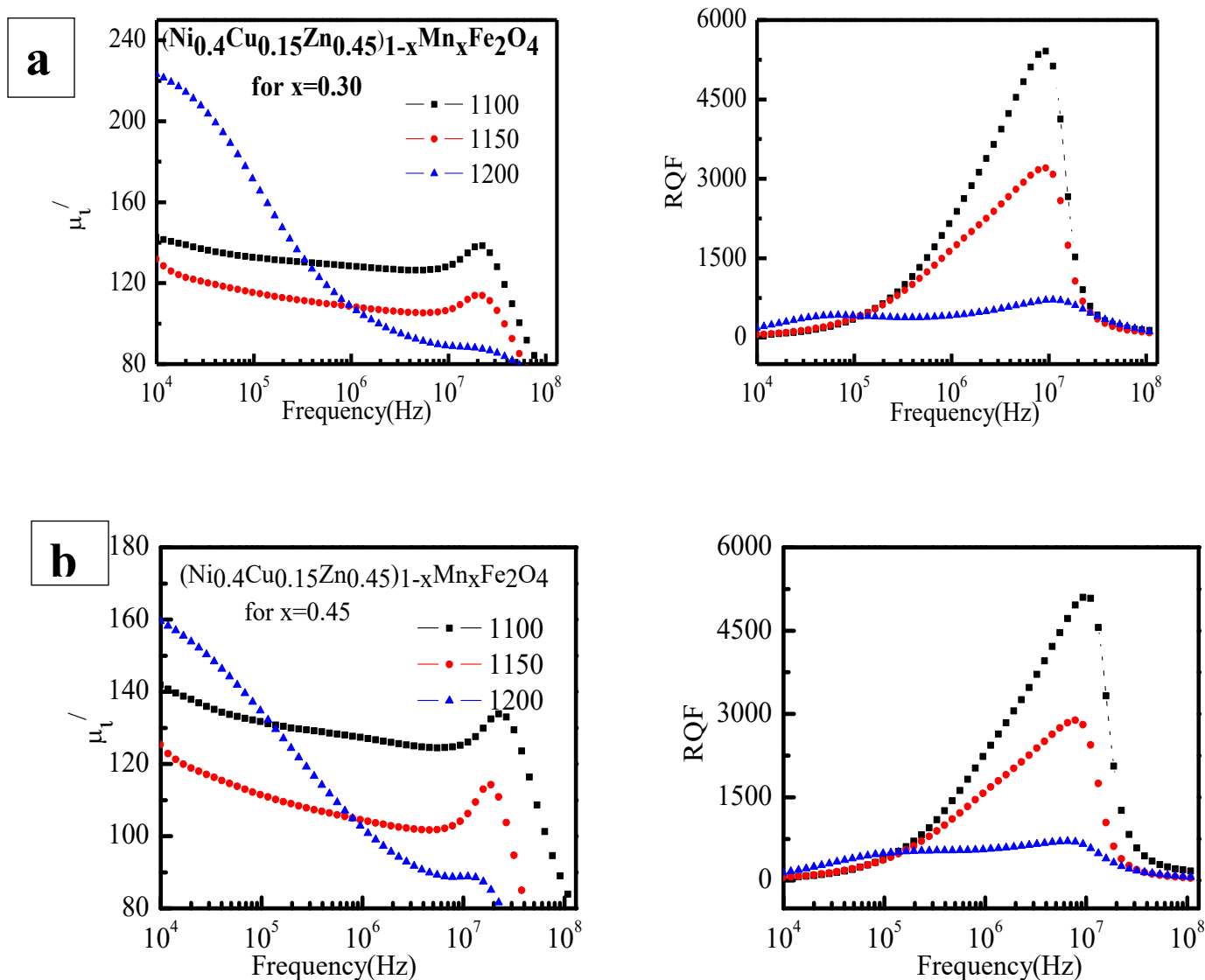

Figure 4.11. The real part and relative quality factor of permeability spectrum for $(Ni_{0.4}Cu_{0.15}Zn_{0.45})_{1-x}Mn_xFe_2O_4$ for (a) x=0.30, (b) x=0.45.

Chapter 5

Conclusions

Compositions of $(Ni_{0.4}Cu_{0.15}Zn_{0.45})_{1-x}Mn_xFe_2O_4$ is successfully prepared by solid state reaction method. The XRD patterns clearly indicate their single phase and formation of spinel structure. Lattice parameter a_o, increases with increase of Mn^{2+} content in $(Ni_{0.4}Cu_{0.15}Zn_{0.45})_{1-x}Mn_xFe_2O_4$. This is due to the fact that Mn^{2+} has an ionic radius of 0.83 Å which replaces Zn^{2+} (0.74 Å), Ni^{2+} (0.69Å) and Cu^{2+} (0.72Å). It is also observed that bulk density and theoretical density decreases with increasing porosity which may have resulted from the replacement of heavier elements (Ni, Zn, Cu have atomic weight of 58.6934(amu), 65.38(amu), 63.546(amu) respectively) with comparatively lighter element (Mn has atomic weight of 54.938 (amu)). The grain size has decreased with increasing Mn content due to porosity. When samples were cooled down, each composition attained completely different physical and chemical properties due to different melting points for different elements that eventually affected the grain size. The EDS result shows the homogeneity of elements in the samples. The initial permeability ($\mu_i^/$) decreases with increasing Mn^{2+} content for temperature 1100, 1150 and 1200^0C. The general characteristic spectra of the real part remain constant in a certain frequency range, but then fall at higher frequencies to a very small value. The resonant frequency f_r alsoincreases with increasing Mn^{2+} content. RQF value found to be the highest for $(Ni_{0.4}Cu_{0.15}Zn_{0.45})_{1-x}Mn_xFe_2O_4$at x=0.30 at 1200^0C.

Recommendations for further research

- More samples of each composition (for each value of x) could have been produced. This would have enhanced the accuracy of the results reducing the error margin.
- More values of x could have been taken for enhanced demonstration of the ferrites characteristics.
- More methods for characterizing the produced samples could have been equipped for greater understanding and analysis.
- The process of ball milling could have been used instead of hand milling; this would have resulted in lesser amount of human errors, including better orientation of the compositions in the mixture
- Lower sintering temperatures should have been taken for achieving greater understanding of permeability and other structural properties of the ferrites.

References

[1] Snoek JL. *New developments in Ferromagnetic Materials* (Elsevier Pub. Co., New York). 1949.

[2] Néel L. *Annales de Physique (Paris) 3, 137*. 1948.

[3] Van Uitert LG. *High-resistivity Nickel Ferrites - The Effect of minor additions of Manganese or Cobalt* J. Chem. Phys. 24, 306. 1956. Available from:http://dx.doi.org/10.1063/1.1742468 [10th October 2017]

[4] Jullien, André; Guinier, Rémi. The Solid State from Superconductors to Superalloys (Pbk. ed.). Oxford: Oxford Univ. Press. ISBN 0198555547. 1989.

[5] Suzuki T, Tanaka T and Ikemizu K. *High density recording capability for advanced particulate media* J. Magn. Magn. Mater. 235, 159. 2001. Available from:http://dx.doi.org/10.1016/S0304-8853(01)00329-8 [13th October 2017]

[6] Olsen E and Thonstad J. *Nickel ferrite as inert anodes in aluminum electrolysis: Part I Material Fabrication and Preliminary Testing* J. Appl. Electrochem. 29, 293. 1999. Available from: http://dx.doi.org/10.1023/A:1003460220418 [14th October 2017]

[7] Ullah Z, Atiq S and Naseem S. *Influence of Pb doping on structural, electrical and magnetic properties of Sr-hexaferrites*. Journal of Alloys and Compounds. 555: 263–267. 2013. Available from: doi: 10.1016/j.jallcom.2012.12.061 [22nd September 2017]

[8]　　Goldman A. *Handbook of Modern Ferromagnetic Materials*, Kulwer Acad. Pub, Boston, U.S.A. 1999

[9]　　Smith J and Wegn. *Ferrites*. John Wiley and Sons Pub., The Netherlands. 1959.

[10]　　Ernst WG. *Earth Materials* (Print ed.). Englewood Cliffs, NJ: Prentice-Hall. p. 58. 1969.

[11]　　National Programme on Technology Enhanced Learning. *Schematic of Spinel Structure.* Available from: http://nptel.ac.in/courses/113104005/lecture3/3_9.htm [21st September 2017]

[12]　　Cullity BD and Graham CD. *Introduction to Magnetic Materials (2nd ed.)*. Wiley-IEEE Press. p. 103. ISBN 0-471-47741-9. 2008.

[13]　　TutorVista. *Electron Spin*. Available from: physics.tutorvista.com/modern-physics/electron-spin.html [1st November 2017]

[14]　　Valenzuela R. *Magnetic Ceramics*, Cambridge University Press, Cambridge. 1994.

[15]   Haque MM. *Influence of additives on the magnetic and electrical properties of iron-excess Mn-Zn ferrites*. M. Phil. Thesis, BUET, Bangladesh. 2000.

[16]   Tasaki J and Ito T, *Intl. Conf. On Ferrite*, Japan. 1970.

[17]   Nakamura T. *Low-temperature sintering of Ni-Zn-Cu ferrite and its permeability spectra*. Journal of Magnetism and Magnetic Materials, **168**, 285. 1997.

[18]   Roess E. *Ferrites*. U. of Tokyo Press, Tokyo, 187. 1971.

[19]   Cullity BD. *Introduction to Magnetic Materials*. Addison-Wiley Publishing Company, Inc., California. 1972.

[20]   Brailsford F. *Physical Principles of Magnetism*. D. Van Nostrand Company Ltd., London. 1966.

[21]   Dekker AJ. *Solid State Physics*. Macmillan India Ltd., New Delhi. 1998.

[22]   Chikazumi S. *Physics of Magnetism*. Jhon Wiley & Sons, Inc., New York. 1966.

[23]   Hadfield D. *Permanent Magnets and Magnetism*. Jhon Wiley & Sons, Inc., New York. 1962.

[24]   Sikder SS. *Temperature dependence of magnetization and induced magnetic anisotropy of some Fe, Co and Ni-based amorphous ribbons*. Ph. D. Thesis, BUET, Bangladesh. 1999.

[25]   Hussain KMA. *Study of complex permeability and secondary effects in some cobalt and manganese based ferrites*. M. Phil. Thesis, BUET, Bangladesh. 2003.

[26]   Kittel C. *Introduction to Solid State Physics*, 7th edition, Jhon Wiley & Sons, Inc., Singapore. 1996.

[27]   Akther Hossain AKM, Seki M, Kawai T and Tabata H. *Colossal magnetoresistance in spinel type $Zn_{1-x}Ni_xFe_2O_4$, J. Appl. Phys.*, **96**, 1273. 2004.

[28]   Kingery WD, Bowen HK and Uhlman DR. *Introduction to Ceramics*, 2nd edition, Wiley Interscience, Newyork, pp. 476. 1976.

[29]   Coble RL and Burke JE, *4th Int. Symp. On the Reactivity of Solids*, Amsterdam, pp. 38-51. 1960.

[30]   McColm J and Clark M. *Forming, Shaping and Working of high Performance Ceramics*, Blackie, Glasgow, pp. 1-338. 1988.

[31]   Stijntjes, Theo & van Loon, Bob. *Early Investigations on Ferrite Magnetic Materials by J. L. Snoek and Colleagues of the Philips Research Laboratories Eindhoven*.

2008. Proceedings of the IEEE. 96. 900-904. 10.1109/JPROC.2008.917767. Available from: https://www.researchgate.net/publication/2998518_Early_Investigations_on_Ferrite_Magnetic_Materials_by_J_L_Snoek_and_Colleagues_of_the_Philips_Research_Laboratories_Eindhoven [22nd December2017]

[32]   Khan M.H.R, Akhtar Hossain A.K.M. Reentrant Spin Glass Behaviour and Large Initial Permeability of $Co_{0.5-x}Mn_xZn_{0.5}Fe_2O_4$ 2012

[33] Akther Hossain AKM, Kabir K.K., Seki M, Kawai T and Tabata H. *Structural, AC and DC Magnetic Properties of $Zn_{1-x}Co_xFe_2O_4$.* 2007.

[34]   Akther Hossain A.K.M and Rahman M.L, "Enhancement of microstructure and initial permeability due to Cu substitution in Ni0.50-xCuxZn0.50Fe2O4 ferrites", Journal of Magnetism and Magnetic Material, Vol 323, Issue 15, 1954-1962, 2011